Supplementary Materials for

Flies Evade Looming Targets by Executing Rapid Visually Directed Banked Turns

Florian T. Muijres, Michael J. Elzinga, Johan Melis, Michael H. Dickinson*

*Corresponding author. E-mail: flyman@uw.edu

Published 11 April 2014, *Science* **344**, 172 (2014)
DOI: 10.1126/science.1248955

This PDF file includes:

Other Supplementary Material for this manuscript includes the following:
(available at www.sciencemag.org/cgi/content/full/344/6180/172/DC1)

Materials and Methods

Experimental Animals

Experiments were performed on 1-5 day old *Drosophila hydei* (males and females), from a laboratory stock reared in a 16:8 (L:D) light cycle. Experimental sessions ran for 5 consecutive days. Each day, we released 50 one-day-old flies in the experimental chamber approximately 10 hours after their subjective dawn and continued recording for 8 hours. Thus, the recording sessions were timed to capture the flies' late crepuscular peak in daily activity. During the experiments, flies were deprived of food and water in order to motivate flight.

Experimental Setup

The experimental setup (Fig. 1) consisted of a transparent cylindrical enclosure (d=h=21 cm). We aligned the two beams of an IR laser triggering system (StopShot, Cognisys Inc) so that they crossed in the middle of the arena. When a fly interrupted both beams, the system triggered both the video recording system and the electronic LED display that provided the visual looming stimulus. The video system consisted of three synchronized high-speed cameras (Photron SA5 with AF Micro Nikkor 60mm lenses), operated with the following parameters: frame rate = 7,500 frames-per-second, exposure time = 1/30,000 seconds, image resolution = 1,024 x 1,024 pixels, image depth = 12 bits, lens aperture = *f*/22. Due to limitations in depth of field, useful data was restricted to a cubic region roughly 40 x 40 x 40 mm in size. The cameras collected images continuously in pre-trigger mode, and when triggered by a fly, stored 372 ms of data before and after the trigger point. For backlighting, we placed a custom built 10 x 10 array of IR LEDs (Vishay VSMY3850-GS08, 850 nm, Fig. S1) on the arena surface opposite each camera. We used a thin diffusing filter in front of each array to create a more homogeneous field of light. The IR LEDs were operated in a pulsed mode using a strobe controller (Gardasoft PP520F), which was triggered by the cameras. The interior of the arena was actively cooled within the range of 24-27°C, by passing cooled air around the outside of the flight chamber using an air-conditioning system (Sunpentown WA1210E).

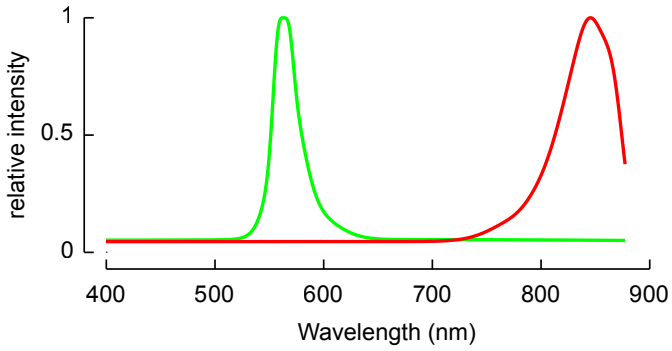

Fig. S1.

The relative intensity distribution throughout the wavelength spectrum for the visual display (green trace) and for the IR backlighting (red trace). Because the visual system of fruit flies is largely insensitive to wavelengths larger than 650 nm (*35*), the strong IR lights required for filming did not affect the flies' ability to see the looming stimulus.

The visual display consisted of a cylindrical array of 192 azimuthal columns and 40 vertical rows of green LEDs (565 nm, Fig. S1) (*14*), with four holes required for the two horizontal cameras and their backlighting arrays. Throughout the experiment, the LEDs were turned on to provide illumination within the arena (70 lux). When triggered, the visual display was programmed to generate a dark expanding circle, with a Michelson contrast of 93% (*14*). The expansion step size was equal to two LEDs in the azimuthal plane (one in each direction), which subtends an angle of 3.75° on the fly's retina when positioned in the center of the arena. The

expansion dynamics could be controlled by varying the stimulus frame rate, step sizes and maximum frame number.

Objects looming with a constant approach generate an exponentially increasing optical angle on the retina of a stationary observer, and thus have a relatively low initial expansion speed. Preliminary tests indicated that, when using this type of stimulus, the flies would leave the recording area before responding, and thus a different stimulus protocol that elicited a response more rapidly was required. Using a stimulus with a constant rate of optical expansion enabled us to decrease the response time to the point that we were able to capture the flies' escape reaction within the measurement volume. Note that a linearly expanding object simulates an object that decelerates during the approach. However, the goal of our study was to investigate the motor reactions of the flies once triggered; an alternate experimental system will be required to study the psychophysics of looming detection in free flying flies.

Analysis of response dynamics

The captured images during escape reactions were analyzed using an automatic machine vision-based tracking system that was custom-built for analyzing *Drosophila* flight dynamics (*15*). Using this system, the body and wings were tracked separately by projecting a fly body model and two wing models onto the three camera images using a DLT method for calibration (*36*). The spatial calibration was based on 112 points positioned within three planes throughout the focal region of the three cameras and was performed at the start and end of every experimental session. The tracking routine output consisted, for each frame, of the 3D position and orientation quaternion of the body ($\boldsymbol{X}=\{x,y,z\}$ and $\boldsymbol{q}_{\text{body}}$) and the orientation quaternion for each wing ($\boldsymbol{q}_{\text{L}}$ and $\boldsymbol{q}_{\text{R}}$). For each flight sequence, body size, wing size and wing hinge locations were initially scaled, and then kept constant throughout the sequence. The $\boldsymbol{X}$ and $\boldsymbol{q}$ time series were post-processed by Kalman filtering the data. For body position, we used a linear Kalman filter. To filter orientation data, we used an extended Kalman filter (*37*) because the quaternion update is non-linear.

The linear Kalman filter provided us with the time dependent vectors of body position, $\boldsymbol{X}(t)$, flight speed, $\boldsymbol{U}(t)$, and body acceleration, $\boldsymbol{a}(t)$, throughout each flight sequence. $\boldsymbol{X}(t)$ and $\boldsymbol{U}(t)$ were used to estimate the flight direction, $\sigma(t)$, and changes in absolute flight speed, ΔU. $\boldsymbol{a}(t)$ was used to estimate force production throughout the maneuver (normalized to body weight) as $F/mg = |\boldsymbol{a}+\boldsymbol{g}|/|\boldsymbol{g}|$. $\boldsymbol{X}(t)$ and $\boldsymbol{a}(t)$ were used to estimate the direction of F/mg relative to the stimulus (σ_{F}). We determined angular velocities of the body, $\boldsymbol{\Omega}=\{\omega_x,\omega_y,\omega_z\}$, from our Kalman estimate of $\boldsymbol{q}_{\text{body}}$. Integrating and differentiating $\boldsymbol{\Omega}$ throughout the maneuver, provided estimates of body roll, pitch, and yaw (φ, θ, and ψ, respectively) throughout the maneuver and their corresponding angular accelerations. Note that we are defining φ, θ, and ψ as the rotation angles around the three axis of the stroke plane (Fig. 1C) rather than the classic Tait-Bryan angles with an Euler rotation scheme, which are commonly used to describe three-dimensional body orientation in flight. The reason for deriving roll, pitch and yaw by integrating angular velocity is because of the order dependence of an Euler angle representation which is misleading with respect to actuation performed in the body reference frame. For example, a maneuver in which a fly consecutively rolls by 90°, pitches up 90°, and then rolls back 90°, results in final Euler angles of 0°, 0° and 90° for roll, pitch and yaw, respectively. Thus, the yaw Euler angle is 90°, although the animal has not generated a yaw maneuver.

The Kalman filtered wing quaternions were used to determine the kinematic angles of the wing. All kinematics angles were defined relative to the plane through the two wing hinges and

set at an angle of 47.5° relative to the longitudinal body axis of the animal. This angle is equal to the average body pitch of *Drosophila* during slow steady flight, and thus defines a horizontal plane through the wing hinges during segments of steady flight (Fig. 1D). The upstroke and downstroke portions of each stroke were determined by the maxima and minima of stroke position. Wingbeat frequency is defined as $1/T$, where T is the time interval between the start of two consecutive downstrokes.

Analysis of wingbeat kinematics

Changes in wingbeat kinematics were correlated with body dynamics by first segmenting all strokes into steady and unsteady classes. A wingbeat was classified as steady or unsteady if the average linear and angular accelerations of the body during the stroke was less than then half the standard deviation of the aggregate acceleration distribution for all sequences. All wingbeats that failed this criterion were classified as unsteady. The resulting relative thresholds were $|\boldsymbol{a}+\boldsymbol{g}|/|\boldsymbol{g}| = 1.10$, $\ddot{\phi}/f^2 = 0.48°$, $\ddot{\theta}/f^2 = 0.29°$, and $\ddot{\psi}/f^2 = 0.27°$, which resulted in a classification of 1603 steady wingbeats and 1963 unsteady wingbeats.

The steady flight wingbeats were used to define the strokeplane angle relative to the body axis (as defined above, equal to the average body pitch angle), and to determine the steady set of wingbeat kinematics by which all maneuvers were compared. In addition to determining an average wingbeat frequency for the steady wingbeat segments, we used Fourier series to fit the time history of stroke angle, deviation angle and rotation angle (Fig. 4A-C and Table S1). The Fourier series were fitted using a Levenberg-Marquardt algorithm and are defined as:

$$k(\tau) = a_0 + \sum_{n=1}^{N} a_n \cos(2\pi n\tau) + b_n \sin(2\pi n\tau), \qquad \text{eq. S1}$$

where k is the specific wingbeat kinematics variable, a_n and b_n are the Fourier series coefficients for the n^{th} order, and τ is normalized time for each wingbeat ($\tau = tf$).

The average body pitch angle and wingbeat frequency for the 1603 steady wingbeats were 47.6°±0.2° (mean±SD) and 188.7±0.5 Hz, respectively. The time series of the angles were fit with an N^{th} order Fourier series, where the order, N, was 4, 8, and 8 for wing stroke angle, rotation angle, and deviation angle respectively (Fig. 4A-C and Table S1). Higher order was required for rotation and deviation because of the higher order harmonics in these signals (Fig. 4B-C).

To analyze the wingbeat kinematics during maneuvers, the unsteady flight dataset was independently parsed into three nonexclusive classes in which the animal significantly increased force production, generated roll torque, or generated pitch torque (up and down). The thresholds for these classes were set at one standard deviation of each respective acceleration distribution ($|\boldsymbol{a}|/|\boldsymbol{g}| = 0.20$; $\ddot{\phi}/f^2 = 0.96°$; and $\ddot{\theta}/f^2 = 0.57°$), resulting in a sets of 719, 582 and 615 wingbeats for increased force production, roll acceleration and pitch acceleration, respectively. For each class, the changes in wingbeat kinematics relative to the steady case were linearly correlated with the measured body accelerations during that stroke in the following way:

$$mod_{k,A,i} = (k_i - k_{\text{steady}}) / (A_i - A_{\text{steady}}), \qquad \text{eq. S2}$$

where $mod_{k,A,i}$ is the wingbeat modification variable for kinematics variable k of the i^{th} wingbeat in the dataset for body acceleration variable A (which includes linear acceleration, roll acceleration, and pitch accelerations). By fitting Fourier series (eq. S1) through the complete dataset of each $mod_{k,A,i}$ (i=1 to I, where I is the number of wingbeats in the dataset), we determined the average wingbeat kinematics distribution, $MOD_{k,A}$, for all combinations of wingbeat kinematics variable, k, and body acceleration variable, A (Table S1). All Fourier series for MOD_{stroke}, $MOD_{rotation}$, and $MOD_{deviation}$, were 8th order (Table S1), while $MOD_{frequency,F/mg}$ was estimated as 41.5±2.7 by a linear fit.

From the $MOD_{k,A}$ estimates, the set of wingbeat kinematics variables that would result in a given type of body acceleration A can be reconstructed by:

$$k = k_{\text{steady}} + \text{MOD}_{k,A} * (A - A_{\text{steady}}). \qquad \text{eq. S3}$$

Note that the kinematics variables for the linear acceleration dataset consist of wing stroke angle, deviation angle, rotation angle and wingbeat frequency, whereas because angular accelerations were normalized using wingbeat frequency squared, frequency was not included as a variable for the roll and pitch maneuvers.

Preliminary analysis on effects of looming parameters

A range of experiments was performed to test the effect of the time course of the looming on the behavioral response. Control experiments in which no expansion was triggered resulted in continuous steady flights, indicating that the flies did not respond to the IR laser trigger system. Providing an expansion stimulus from two opposite sides of the arena did not reveal any bias in response dynamics relative to the geometry of the setup. We used three different constant expansion speeds in these experiments: 0.65° ms^{-1}, 1.3° ms^{-1} and 2.1° ms^{-1}.

Using an expectation maximization-based clustering analysis on the linear acceleration data of all flight sequences, we defined the start of the response at a linear acceleration threshold of 0.28 g. Based on this threshold, the response times were 84±17 ms (n=18), 75±10 ms (n=34) and 43±8 ms (n=44) for the looming stimuli with slow, medium and fast expansion speed, respectively. Although response time is significantly faster for the faster stimulus, the response dynamics were identical if temporally aligned according to an acceleration threshold of 0.28 g (Fig. 2H and Fig. 3K). We also tested three different maximum stimulus expansion angles (χ_{max} = 32°, 64° and 165°), in combination with two post expansion conditions (either turning all LEDs directly on after the dark stimulus reaches maximum size or having the dark stimulus to remain present). Again, we did not find any significant differences in escape dynamics under these six different conditions. Based on these preliminary findings, our subsequent analysis was based on the assumption that, once triggered, the motor reaction we measured were dependent on the azimuthal position of the stimulus but not on the time course of stimulus expansion.

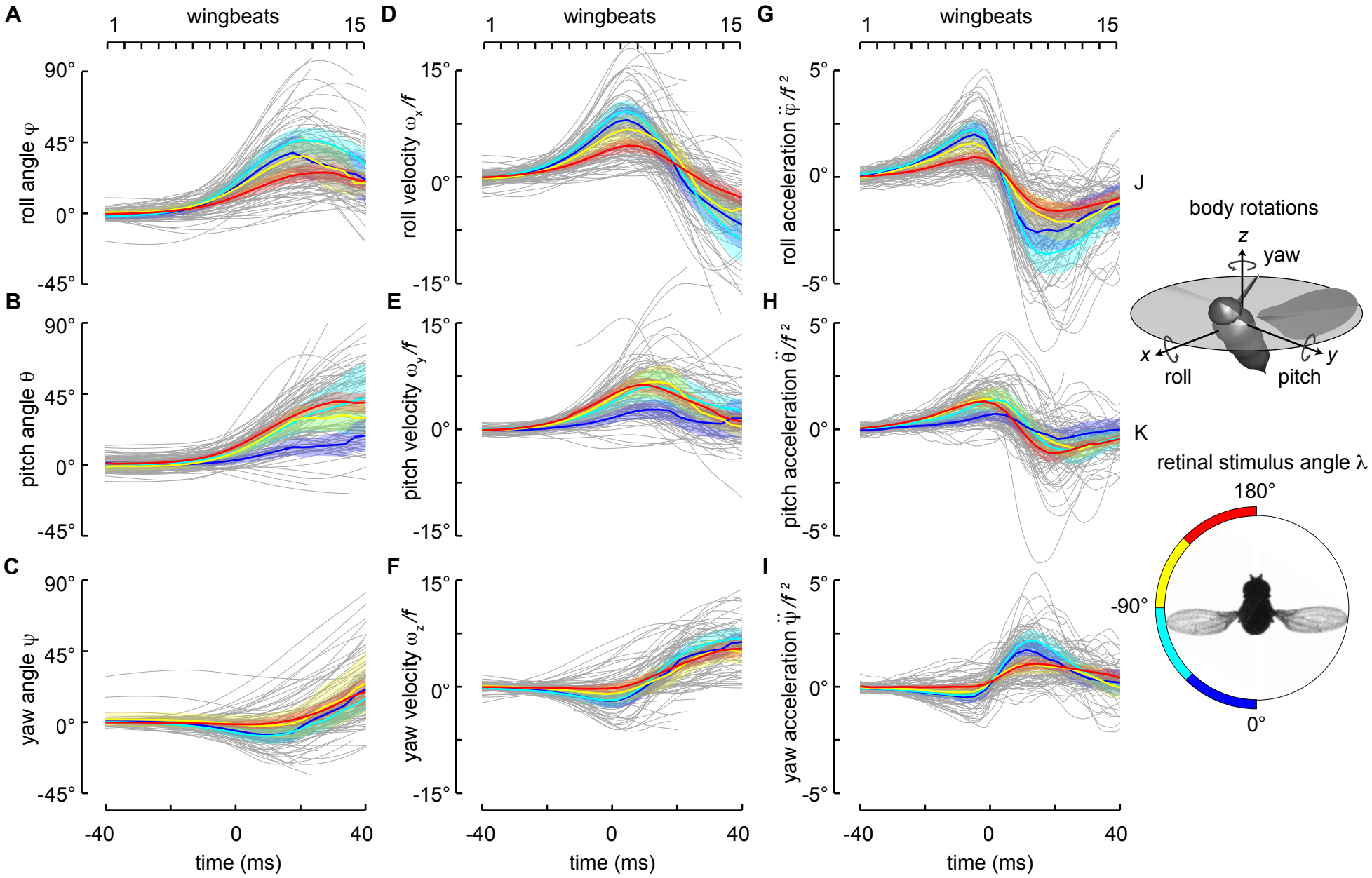

Fig. S2. Flies steer away from looming stimuli by performing banked turns. (A-C) Time history of body angles aligned to start of motor response: (A) roll, ϕ; (B) pitch, θ; (C) yaw, ψ (D-F) Time history for body angle velocities normalized by wingbeat frequency f: (D) roll rate, ω_x/f; (E) pitch rate, ω_y/f; (F) yaw rate, ω_z/f. (G-I) Time history for body angle accelerations normalized by the square of wingbeat frequency f: (G) roll acceleration, $\ddot{\varphi}/f^2$; (H) pitch acceleration, $\ddot{\theta}/f^2$; (I) yaw acceleration, $\ddot{\psi}/f^2$. Body angles and their derivatives are defined as in (J). In A-I, thin grey lines indicate separate flight sequences; colored lines and shaded areas are average and 95% confidence intervals for four subsets of data in which the flies were approached from different 45°–wide azimuthal sectors (K).

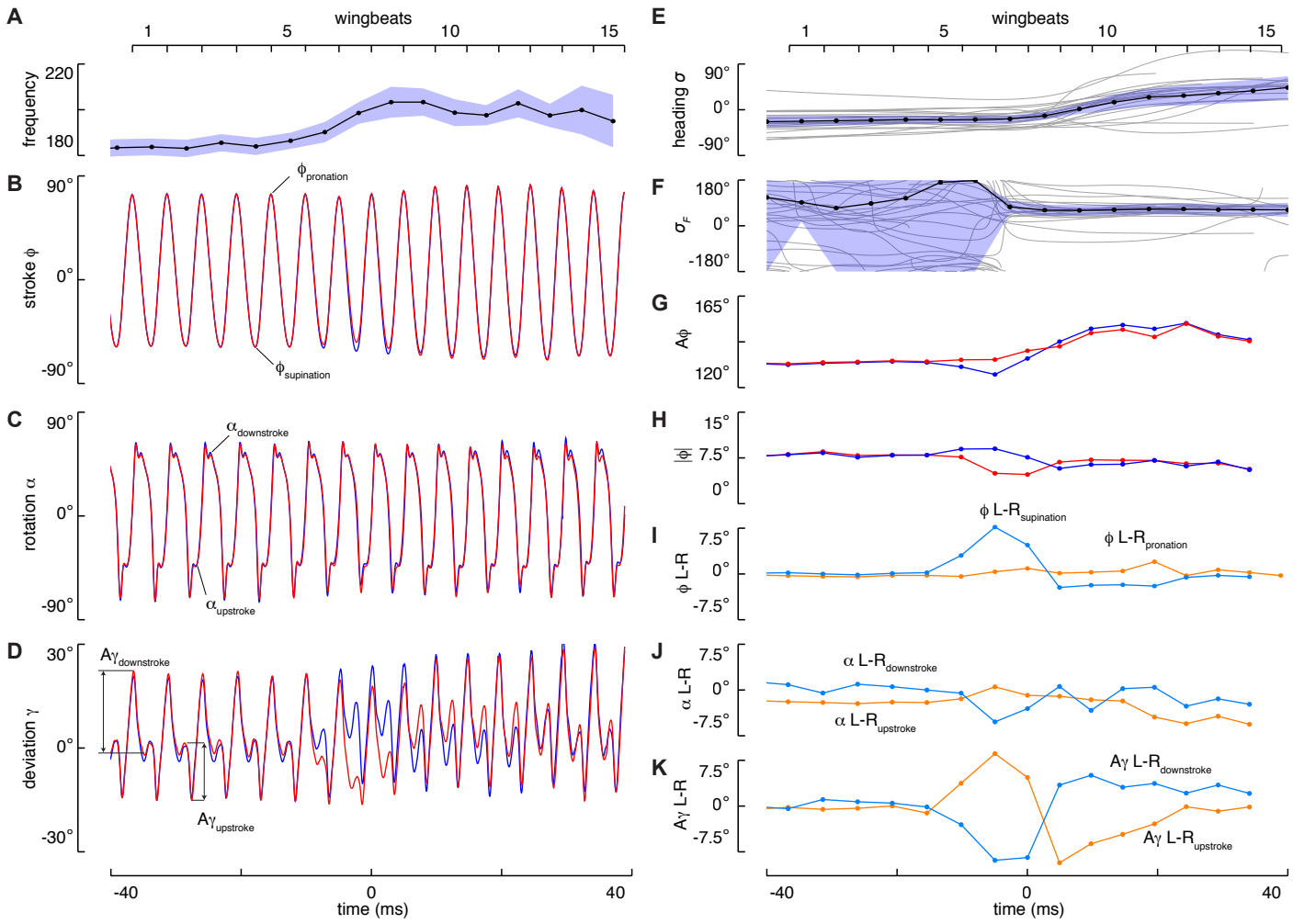

Fig. S3. Average wingbeat kinematics and turn dynamics throughout the escape maneuver for the 21 flies that received the looming stimulus in the first azimuthal sector of the retinal stimulus angle (λ>-45°), as defined in the top left inset in Fig. 2G. See Fig. 1D for wingbeat angle definitions. (A) f, flapping frequency; (B) φ, stroke angle of the left (blue) and right (red) wing; (C) α, rotation angle of the left (blue) and right (red) wing; (D) γ, deviation angle of the left (blue) and right (red) wing. (E) σ, heading in the stimulus reference frame; (F) σ_F, the direction of the horizontal aerodynamic force component in the stimulus reference frame; (G) Aφ, stroke angle amplitude of the left (blue) and right (red) wing; (H) $|\varphi|$, wingbeat mean stroke angle of the left (blue) and right (red) wing; (I) φ L-R, difference between the left wing stroke angle and the right wing stroke angle, at the end of the downstroke (at wing supination, light blue), and at the end of the upstroke (at wing pronation, orange); (J) α L-R, difference between the left wing rotation angle and the right wing rotation angle, at mid downstroke (light blue), and at mid upstroke (orange); (K) Aγ L-R, difference between the left wing deviation angle amplitude and the right wing deviation angle amplitude, for the downstroke (light blue), and for the upstroke (orange). In (A,E-K), points indicate the mean values for the specific wingbeat, shaded areas are 95% confidence intervals, and thin grey lines indicate separate flight sequences.

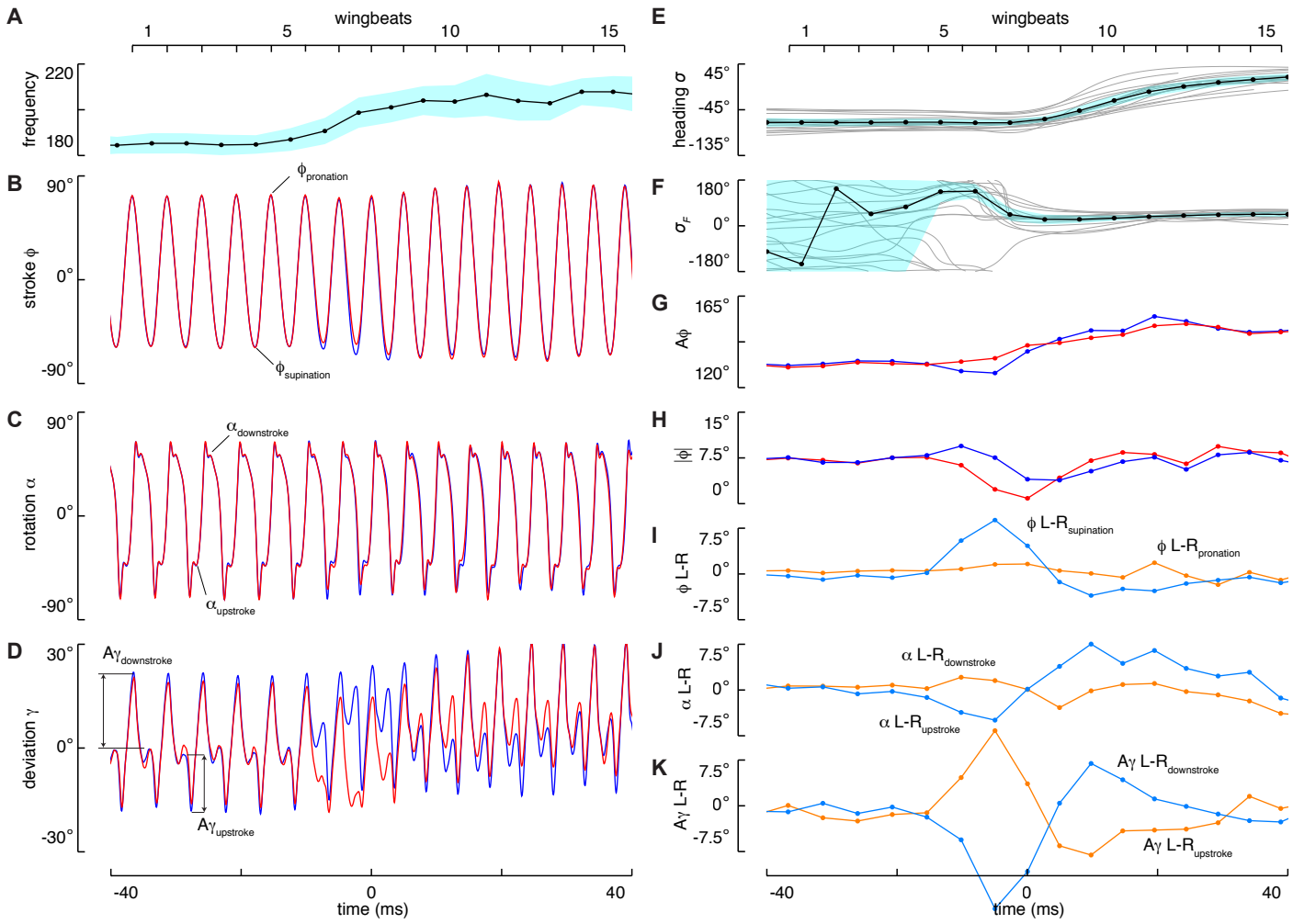

Fig. S4. Average wingbeat kinematics and turn dynamics throughout the escape maneuver for the 16 flies that received the looming stimulus in the second azimuthal sector of the retinal stimulus angle ($-90^{o}<\lambda<-45^{o}$), as defined in the top left inset in Fig. 2G. See Fig. 1D for wingbeat angle definitions. See Fig. S2 for a detailed description of the variables in each panel.

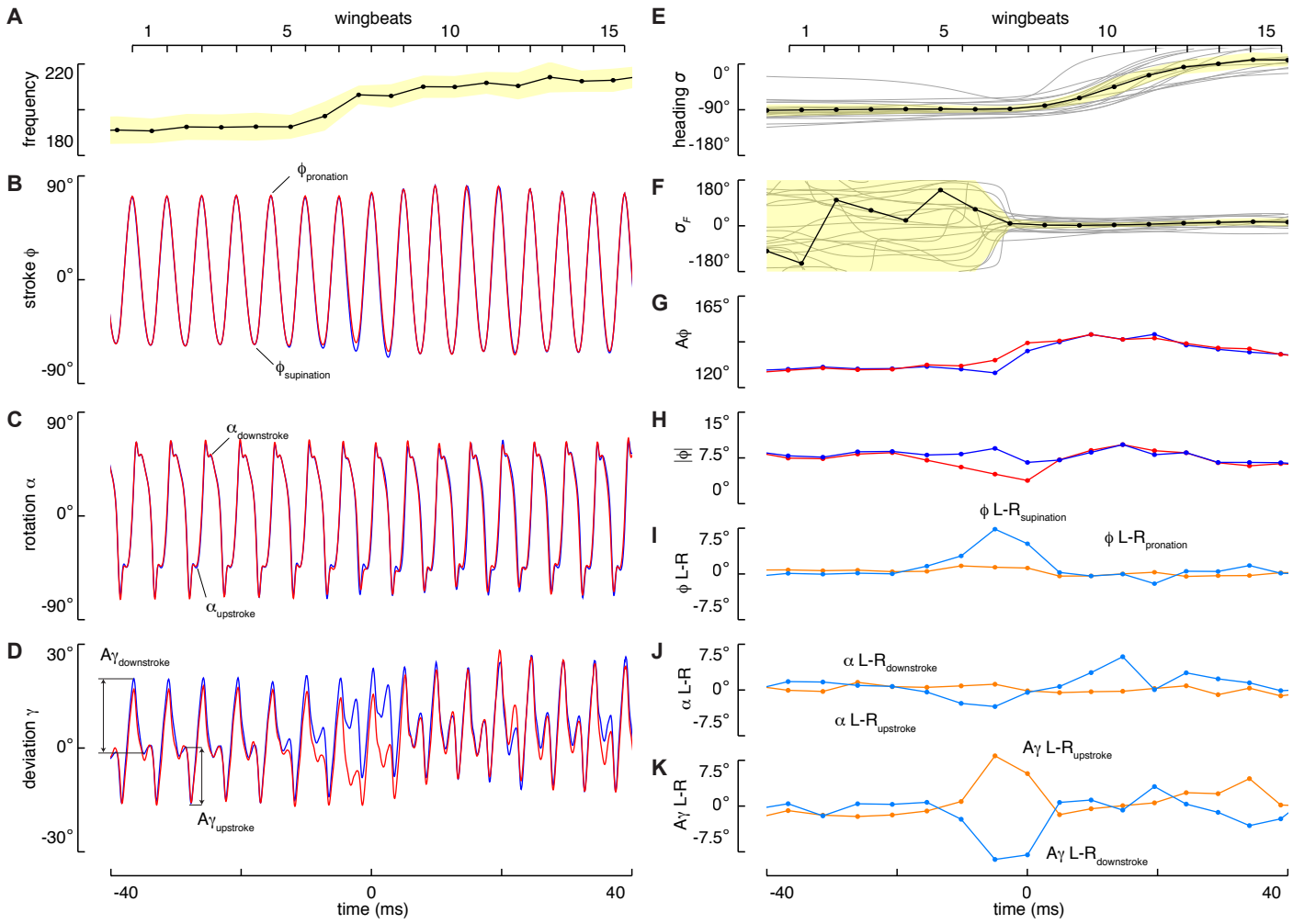

Fig. S5. Average wingbeat kinematics and turn dynamics throughout the escape maneuver for the 17 flies that received the looming stimulus in the second azimuthal sector of the retinal stimulus angle ($-135^{o}<\lambda<-90^{o}$), as defined in the top left inset in Fig. 2G. See Fig. 1D for wingbeat angle definitions. See Fig. S2 for a detailed description of the variables in each panel.

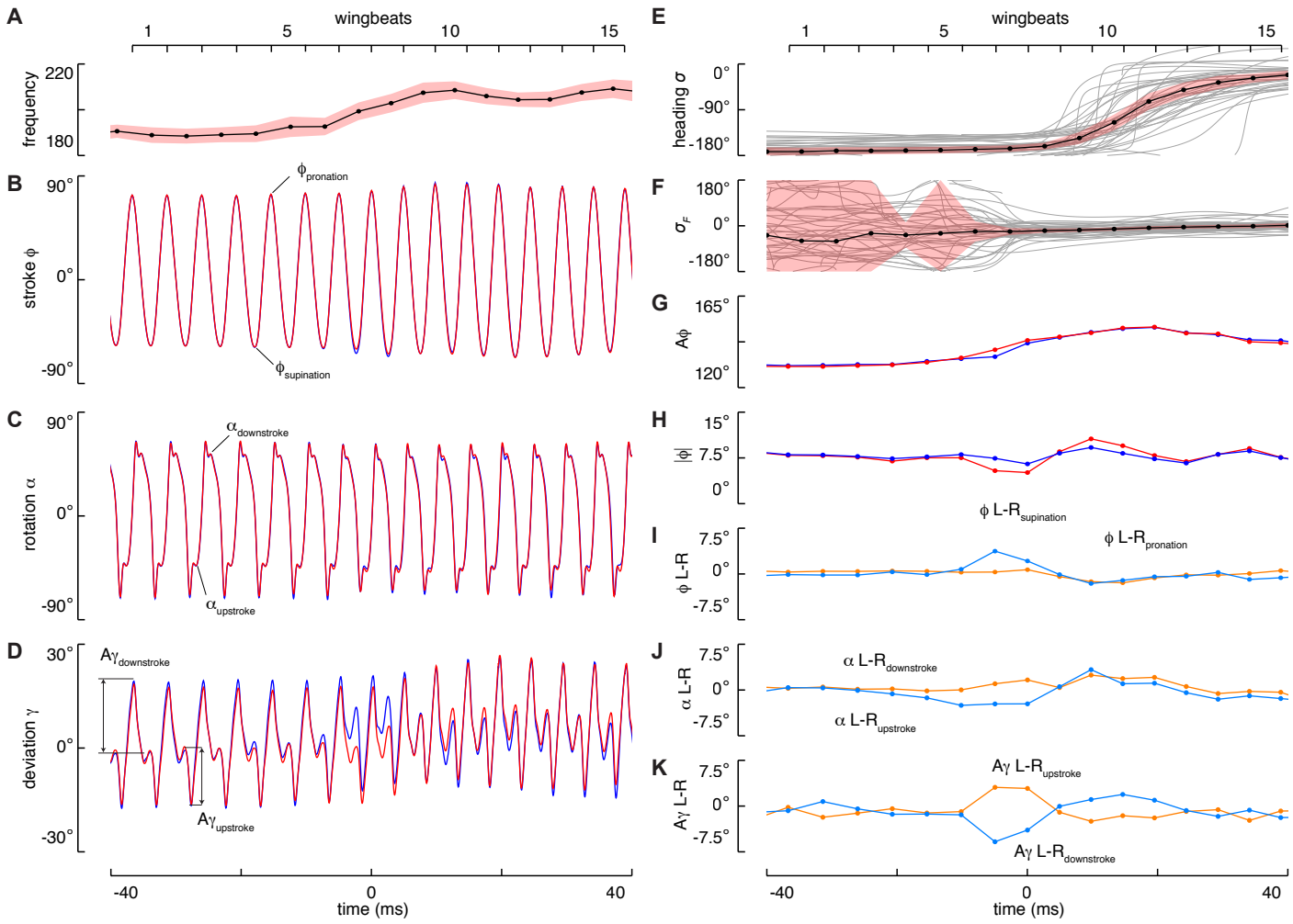

Fig. S6. Average wingbeat kinematics and turn dynamics throughout the escape maneuver for the 38 flies that received the looming stimulus in the second azimuthal sector of the retinal stimulus angle (λ<-135^o), as defined in the top left inset in Fig. 2G. See Fig. 1D for wingbeat angle definitions. See Fig. S2 for a detailed description of the variables in each panel.

Table S1.

Coefficients and statistical data of the Fourier series (eq. S1) for the steady wingbeats and the wingbeat modulations that govern linear body accelerations, body pitch angle accelerations, and body roll accelerations, respectively. For the laterally asymmetric body roll case, the wingbeat kinematics for the upwards and downwards accelerating wings are provided separately.

Steady wingbeat kinematics

	stroke		***rotation***		***deviation***	
N	a_n	b_n	a_n	b_n	a_n	b_n
0	3.9008	-	4.2936	-	-6.173	-
1	65.0445	4.2642	1.8536	59.6529	6.5682	3.7788
2	3.5806	-2.9492	5.1852	1.6095	6.1335	0.8717
3	0.1319	0.3639	-8.4569	9.8057	-0.352	-0.6606
4	0.7844	0.2098	3.9562	5.8064	0.0447	1.2816
5	-	-	-3.0337	-2.8749	0.5257	0.3556
6	-	-	-2.8771	0.6686	-0.3202	-0.2039
7	-	-	0.8649	-0.6137	-0.2993	0.1891
8	-	-	0.0771	-1.0007	0.0221	0.0379
n	1603		1603		1603	
sse	8.0627		8.4016		1.1506	
r^2	1.0000		1.0000		0.9999	
dfe	191		183		183	
adj r^2	1.0000		1.0000		0.9999	
rmse	0.2055		0.2143		0.0793	

Linear acceleration modulation

	stroke		***rotation***		***deviation***	
n	a_n	b_n	a_n	b_n	a_n	b_n
0	-4.6736	-	-4.9784	-	7.1015	-
1	14.1313	0.9415	-4.374	1.6273	-2.472	-1.7041
2	3.1407	1.4655	-6.4068	0.25	3.0183	1.5893
3	0.4728	-0.9957	-0.6567	-0.8134	0.7339	-1.459
4	-0.5968	-0.2136	-5.4767	-1.8678	-0.0375	-0.1021
5	0.496	-0.0093	1.0895	1.4223	-0.0355	0.538
6	0.1765	-0.5429	2.1159	-2.5199	0.0913	0.2958
7	-0.075	-0.0503	-0.571	0.2408	0.0906	-0.3932
8	0.0697	0.0249	0.5521	1.2054	-0.0734	-0.2456
n	719		719		719	
sse	2.8074		3.8553		2.1145	
r^2	0.9996		1.0000		0.9976	
dfe	183		183		183	
adj r^2	0.9996		1.0000		0.9974	
rmse	0.1239		0.1451		0.1075	

Pitch acceleration modulation

	stroke		***rotation***		***deviation***	
n	a_n	b_n	a_n	b_n	a_n	b_n
0	-0.8131	-	-0.4648	-	-0.7202	-
1	-1.2546	-1.4999	1.2876	-0.2763	-0.2447	0.7053
2	-0.2231	0.0246	-0.625	-0.2962	-0.4336	-0.4589
3	-0.1089	0.0404	0.1871	0.7462	-0.2864	0.1155
4	0.0222	-0.047	0.5042	-0.6062	0.0741	-0.0279
5	-0.0943	-0.0392	-0.4812	-0.0057	-0.0274	-0.208
6	-0.0271	0.0054	0.1589	0.3995	-0.07	-0.0455
7	-0.0072	-0.0281	0.1162	-0.1608	0.0257	0.0235
8	-0.0234	-0.059	-0.0801	0.0538	0.0187	-0.0137
n	615		615		615	
sse	8.3671		6.0312		0.8054	
r^2	1.0000		1.0000		0.9999	
dfe	191		183		183	
adj r^2	1.0000		1.0000		0.9999	
rmse	0.2093		0.1815		0.0663	

Roll acceleration modulation for upward accelerating wing

	stroke		***rotation***		***deviation***	
n	a_n	b_n	a_n	b_n	a_n	b_n
0	-1.1948	-	-0.7681	-	1.817	-
1	2.4902	0.0574	0.0325	0.1112	-0.8097	-0.2229
2	0.5719	0.3229	-1.2837	-0.2991	0.5658	0.1953
3	0.066	-0.1568	0.2203	0.1268	0.0103	-0.305
4	-0.1224	-0.0279	-0.7092	-0.5942	0.0402	-0.0265
5	0.0767	0.0137	0.0541	0.3131	0.0194	0.0347
6	0.0294	-0.076	0.3676	-0.2498	0.0158	0.0468
7	-0.0147	-0.0057	-0.1034	-0.0118	0.0227	-0.0735
8	0.0079	0.0059	0.0000	0.2286	-0.0254	-0.0602
n	582		582		582	
sse	1.0608		14.1114		3.2721	
r^2	0.9998		0.9945		0.9966	
dfe	183		183		183	
adj r^2	0.9998		0.9940		0.9964	
rmse	0.0761		0.2777		0.1337	

Roll acceleration modulation for downward accelerating wing

	stroke		***rotation***		***deviation***	
n	a_n	b_n	a_n	b_n	a_n	b_n
0	-0.3819	-	-0.4162	-	0.5095	-
1	1.7718	0.4261	-1.8177	0.1848	0.4199	-0.4118
2	0.4062	0.2757	-0.589	0.2037	0.3139	0.1942
3	0.1439	-0.1749	-0.3515	-0.6688	0.1248	-0.2259
4	-0.0419	-0.0021	-1.2698	0.0813	-0.0941	-0.0825
5	0.1107	0.0032	0.4239	0.2272	-0.0476	0.17
6	0.0324	-0.0849	0.327	-0.5451	0.0555	0.0747
7	-0.0202	0.0049	-0.134	0.0473	-0.0022	-0.0679
8	0.0129	0.0126	0.1257	0.2061	-0.0261	-0.0161
n	582		582		582	
sse	1.1801		11.7784		1.2755	
r^2	0.9996		0.9979		0.9975	
dfe	183		183		183	
adj r^2	0.9996		0.9977		0.9973	
rmse	0.0803		0.2537		0.0835	

Movie S1

High-speed video corresponding to photomontage in Fig. 1E(a). Sequence was filmed at 7500 frames per second, but is replayed at 300x slower speed. The sequence begins at the point that the visual stimulus begins to expand. The stimulus approaches fly from bottom right.

Movie S2

High-speed video corresponding to photomontage in Fig. 1E(b). Sequence was filmed at 7500 frames per second, but is replayed at 300x slower speed. The sequence begins at the point that the visual stimulus begins to expand. The stimulus approaches fly from bottom right.

Movie S3

High-speed video corresponding to photomontage in Fig. 1E(c). Sequence was filmed at 7500 frames per second, but is replayed at 300x slower speed. The sequence begins at the point that the visual stimulus begins to expand. The stimulus approaches fly from bottom right.

Movie S4

High-speed video corresponding to photomontage in Fig. 1E(d). Sequence was filmed at 7500 frames per second, but is replayed at 300x slower speed. The sequence begins at the point that the visual stimulus begins to expand. The stimulus approaches fly from bottom right.

Movie S5

High-speed video corresponding to photomontage in Fig. 1E(e). Sequence was filmed at 7500 frames per second, but is replayed at 300x slower speed. The sequence begins at the point that the visual stimulus begins to expand. The stimulus approaches fly from bottom right.

Movie S6

High-speed video corresponding to photomontage in Fig. 1E(f). Sequence was filmed at 7500 frames per second, but is replayed at 300x slower speed. The sequence begins at the point that the visual stimulus begins to expand. The stimulus approaches fly from bottom right.

Movie S7

Example tracking result of a full trajectory showing a fly's response to a looming stimulus in two reference frames: the lab frame (left) and a frame that follows the fly's center of mass (right).

Movie S8

An animated cartoon illustrating the changes in wing and body motion on a stroke-by-stroke basis from four different views. The data are the same as presented in Supplementary Movie 7. Each frame of the movie shows a single wingstroke.

Movie S9

Animated version of the wingstrokes depicted in Fig. 5A. Grey and black wing chords represent patterns generating steady flight and peak flight force, respectively.

Movie S10

Animated version of the wingstrokes depicted in Fig. 5B. Grey and black wing chords represent patterns of right and left wings during production of peak roll acceleration, respectively.

Movie S11

Animated version of the wingstrokes depicted in Fig. 5C. Grey and black wing chords represent patterns generating peak nose down and nose up pitch acceleration, respectively.

Database S1

Compressed MATLAB (MathWorks, Inc.) database with information about all reported flight trials, and with results from the robotic fly experiments. The flight trial data consisted of information about the experimental setup and conditions and body and wing kinematics data throughout each flight sequences. Body kinematics consist of the position $\boldsymbol{X}$, velocity $\boldsymbol{U}$, acceleration $\boldsymbol{a}$, orientation $\boldsymbol{q}_{\text{body}}$ and angular velocities $\boldsymbol{\Omega}$ of the body at each point in time t. Wingbeat kinematics are described by the corresponding stroke angle ϕ, deviation angle γ and rotation angle α of both wings with length l and wing joint location $\boldsymbol{x}_{\text{joint}}$ (in the body reference frame). Looming stimulus data provides the optical angle of the expanding circle in the flies' reference frame for each point in time t. Body and wing model data are provided as a series of node points and scaling parameters (15). The robotic fly data consisted of the temporal dynamics of the wingbeat kinematics angles (as defined in Fig. 1D and constructed using eq. S3) and forces and torques about the three body axes (as defined in Fig. 1C), for all data reported in Fig. 6 (i.e. wingbeats that result in linear acceleration, roll angle acceleration, and pitch angle acceleration). The measured forces and torques were converted to fly scales (using dynamic scaling) and normalized; both the unfiltered and Butterworth filtered data are provided.

References

1. A. Borst, J. Haag, D. F. Reiff, Fly motion vision. *Annu. Rev. Neurosci.* **33**, 49–70 (2010). doi:10.1146/annurev-neuro-060909-153155 Medline

2. M. S. Tu, M. H. Dickinson, The control of wing kinematics by two steering muscles of the blowfly (*Calliphora vicina*). *J. Comp. Physiol. A.* **178**, 813–830 (1996). doi:10.1007/BF00225830 Medline

3. F.-O. Lehmann, in *Nature's Versatile Engine: Insect Flight Muscle Inside and Out*, J. O. Vigoreaux, Ed. (Landes Bioscience/Eurekah.com, Georgetown, TX, 2006), pp. 230–239.

4. M. A. Frye, M. H. Dickinson, Fly flight: A model for the neural control of complex behavior. *Neuron* **32**, 385–388 (2001). doi:10.1016/S0896-6273(01)00490-1 Medline

5. M. H. Dickinson, F.-O. Lehmann, S. P. Sane, Wing rotation and the aerodynamic basis of insect flight. *Science* **284**, 1954–1960 (1999). doi:10.1126/science.284.5422.1954 Medline

6. M. H. Dickinson, K. Götz, Unsteady aerodynamic performance of model wings at low Reynolds numbers. *J. Exp. Biol.* **174**, 45–64 (1993).

7. L. Ristroph, G. J. Berman, A. J. Bergou, Z. J. Wang, I. Cohen, Automated hull reconstruction motion tracking (HRMT) applied to sideways maneuvers of free-flying insects. *J. Exp. Biol.* **212**, 1324–1335 (2009). doi:10.1242/jeb.025502 Medline

8. G. Card, M. H. Dickinson, Visually mediated motor planning in the escape response of *Drosophila*. *Curr. Biol.* **18**, 1300–1307 (2008). doi:10.1016/j.cub.2008.07.094 Medline

9. S. A. Combes, D. E. Rundle, J. M. Iwasaki, J. D. Crall, Linking biomechanics and ecology through predator-prey interactions: Flight performance of dragonflies and their prey. *J. Exp. Biol.* **215**, 903–913 (2012). doi:10.1242/jeb.059394 Medline

10. K. G. Götz, Optomotorische untersuchung des visuellen systems einiger augenmutanten der fruchtfliege *Drosophila*. *Kybernetik* 77–92 (1964). doi:10.1007/BF00288561

11. T. L. Hedrick, B. Cheng, X. Deng, Wingbeat time and the scaling of passive rotational damping in flapping flight. *Science* **324**, 252–255 (2009). doi:10.1126/science.1168431 Medline

12. A. J. Bergou, L. Ristroph, J. Guckenheimer, I. Cohen, Z. J. Wang, Fruit flies modulate passive wing pitching to generate in-flight turns. *Phys. Rev. Lett.* **104**, 148101 (2010). doi:10.1103/PhysRevLett.104.148101 Medline

13. Materials and methods are available as supplementary materials on *Science* Online.

14. M. B. Reiser, M. H. Dickinson, A modular display system for insect behavioral neuroscience. *J. Neurosci. Methods* **167**, 127–139 (2008). doi:10.1016/j.jneumeth.2007.07.019 Medline

15. E. I. Fontaine, F. Zabala, M. H. Dickinson, J. W. Burdick, Wing and body motion during flight initiation in *Drosophila* revealed by automated visual tracking. *J. Exp. Biol.* **212**, 1307–1323 (2009). doi:10.1242/jeb.025379 Medline

16. S. E. J. de Vries, T. R. Clandinin, Loom-sensitive neurons link computation to action in the *Drosophila* visual system. *Curr. Biol.* **22**, 353–362 (2012). doi:10.1016/j.cub.2012.01.007 Medline

17. J. A. Bender, M. H. Dickinson, Visual stimulation of saccades in magnetically tethered *Drosophila*. *J. Exp. Biol.* **209**, 3170–3182 (2006). doi:10.1242/jeb.02369 Medline

18. M. B. Reiser, M. H. Dickinson, Visual motion speed determines a behavioral switch from forward flight to expansion avoidance in *Drosophila*. *J. Exp. Biol.* **216**, 719–732 (2013). doi:10.1242/jeb.074732 Medline

19. H. Fotowat, F. Gabbiani, Collision detection as a model for sensory-motor integration. *Annu. Rev. Neurosci.* **34**, 1–19 (2011). doi:10.1146/annurev-neuro-061010-113632 Medline

20. C. David, The relationship between body angle and flight speed in free-flying *Drosophila*. *Physiol. Entomol.* **3**, 191–195 (1978). doi:10.1111/j.1365-3032.1978.tb00148.x

21. K. G. Götz, U. Wandel, Optomotor control of the force of flight in *Drosophila* and *Musca*. *Biol. Cybern.* **51**, 135–139 (1984). doi:10.1007/BF00357927

22. S. Vogel, Flight in *Drosophila*: I. Flight performance of tethered flies. *J. Exp. Biol.* **44**, 567–578 (1966).

23. S. N. Fry, R. Sayaman, M. H. Dickinson, The aerodynamics of free-flight maneuvers in *Drosophila*. *Science* **300**, 495–498 (2003). doi:10.1126/science.1081944 Medline

24. P. Domenici, J. M. Blagburn, J. P. Bacon, Animal escapology I: Theoretical issues and emerging trends in escape trajectories. *J. Exp. Biol.* **214**, 2463–2473 (2011). doi:10.1242/jeb.029652 Medline

25. M. J. Elzinga, W. B. Dickson, M. H. Dickinson, The influence of sensory delay on the yaw dynamics of a flapping insect. *J. R. Soc. Interface* **9**, 1685–1696 (2012). doi:10.1098/rsif.2011.0699 Medline

26. J. A. Bender, M. H. Dickinson, A comparison of visual and haltere-mediated feedback in the control of body saccades in *Drosophila melanogaster*. *J. Exp. Biol.* **209**, 4597–4606 (2006). doi:10.1242/jeb.02583 Medline

27. L. Ristroph, A. J. Bergou, G. Ristroph, K. Coumes, G. J. Berman, J. Guckenheimer, Z. J. Wang, I. Cohen, Discovering the flight autostabilizer of fruit flies by inducing aerial stumbles. *Proc. Natl. Acad. Sci. U.S.A.* **107**, 4820–4824 (2010). doi:10.1073/pnas.1000615107 Medline

28. A. Sherman, M. H. Dickinson, A comparison of visual and haltere-mediated equilibrium reflexes in the fruit fly *Drosophila melanogaster*. *J. Exp. Biol.* **206**, 295–302 (2003). doi:10.1242/jeb.00075 Medline

29. W. B. Dickson, P. Polidoro, M. M. Tanner, M. H. Dickinson, A linear systems analysis of the yaw dynamics of a dynamically scaled insect model. *J. Exp. Biol.* **213**, 3047–3061 (2010). doi:10.1242/jeb.042978 Medline

30. B. Cheng, X. Deng, Translational and rotational damping of flapping flight and its dynamics and stability at hovering. *IEEE Trans. Robot.* **27**, 849–864 (2011). doi:10.1109/TRO.2011.2156170

31. F.-O. Lehmann, M. H. Dickinson, The changes in power requirements and muscle efficiency during elevated force production in the fruit fly *Drosophila melanogaster*. *J. Exp. Biol.* **200**, 1133–1143 (1997). Medline

32. M. H. Dickinson, Haltere-mediated equilibrium reflexes of the fruit fly, *Drosophila melanogaster*. *Philos. Trans. R. Soc. Lond. B Biol. Sci.* **354**, 903–916 (1999). doi:10.1098/rstb.1999.0442 Medline

33. L. F. Tammero, M. H. Dickinson, The influence of visual landscape on the free flight behavior of the fruit fly *Drosophila melanogaster*. *J. Exp. Biol.* **205**, 327–343 (2002). Medline

34. F. van Breugel, M. H. M. Dickinson, The visual control of landing and obstacle avoidance in the fruit fly *Drosophila melanogaster*. *J. Exp. Biol.* **215**, 1783–1798 (2012). doi:10.1242/jeb.066498 Medline

35. C. Schnaitmann, C. Garbers, T. Wachtler, H. Tanimoto, Color discrimination with broadband photoreceptors. *Curr. Biol.* **23**, 2375–2382 (2013). doi:10.1016/j.cub.2013.10.037 Medline

36. R. Hartley, A. Zisserman, *Multiple View Geometry in Computer Vision* (Cambridge Univ. Press, Cambridge, UK, 2000).

37. X. Yun, E. R. Bachmann, Design, implementation, and experimental results of a quaternion-based Kalman filter for human body motion tracking. *IEEE Trans. Robot.* **22**, 1216–1227 (2006). doi:10.1109/TRO.2006.886270